Article

Single-Impact Failure of Multi-Layered Automotive Coatings: A Finite Element-Based Study

Li Chen [1], **Chenqi Zou** [1], **Mengyan Zang** [1,*] **and Shunhua Chen** [2,3,*]

[1] School of Mechanical & Automotive Engineering, South China University of Technology, Guangzhou 510641, China
[2] School of Marine Engineering and Technology, Sun Yat-sen University, Zhuhai 519082, China
[3] Southern Marine Science and Engineering Guangdong Laboratory (Zhuhai), Zhuhai 519082, China
* Correspondence: myzang@scut.edu.cn (M.Z.); chenshh73@mail.sysu.edu.cn (S.C.)

Abstract: Automotive coatings are a multi-layered polymer composite structure whose impact resistance is closely related to the appearance and safety of a vehicle. Since experimental methods are of high cost and poor repeatability, in our work, a finite element model is developed for the single-impact failure of automotive coatings. In this model, a multi-mechanism damage model and a large deformation cohesive zone model are employed to account for the polymer-ply and interlaminar failures of the coating, and some rate-dependent material models are adopted to capture the effect of impact velocity. The simulated results indicate that the proposed model can reproduce the failure patterns of automotive coatings well. In addition, the impact failure mechanisms of the coating are revealed. Numerical findings show that both brittle and ductile failures are found in the coating and there are three stages for the propagation of the delamination crack. Finally, we numerically investigate the effects of primer mechanical properties, i.e., Young's modulus, yield strength, and re-hardening modulus, on the impact resistance of automotive coatings. Our work is helpful to the design of coating, which can improve the impact resistance of automotive coatings.

Keywords: automotive coating; numerical study; continuum damage model; cohesive zone model; impact failure mechanism

1. Introduction

Automotive coatings are a typical multi-layered polymer composite structure, which usually consists of four paint films, i.e., the clearcoat, basecoat, primer, and electrocoat. During the service life of a vehicle, particle impacts are inevitable, which lead to mechanical damage of the coating. Minor damage is just an aesthetic problem, but severe damage means that the material under the coating is exposed, causing corrosion to metal parts, which affects the safety performance of the vehicle. In light of this, it is of great significance for traveling safety to study the impact failure characteristics of automotive coatings, which has concerned researchers and related enterprises.

The experimental methods for the impact resistance of automotive coatings include both multi- and single-particle impact tests. Two experimental standards have been proposed for multi-particle impact tests, i.e., the DIN 55996-1:2001 [1] and the SAE J400 [2]. Through the multi-particle tests, Huang [3] qualitatively evaluated the impact resistance of an automotive coating sample. The effect of paint layer thickness on erosion resistance was also investigated for two acrylic automotive topcoats by Trezona et al. [4]. To avoid the subjective evaluation inherent in these standards, some new indicators and measurement methods have been proposed [5–7]. Although the resistance of automotive coatings to stone strike can be rapidly evaluated through the multi-particle impact tests, it is not conducive to parameter studies due to the complex impact conditions. Therefore, more researchers prefer single-particle impact tests to study the impact event. Nichols et al. [8] quantified the influences of impact angle and particle geometry by the lost material volume.

The dependence of impact damage area on coating thickness and contact type had also been experimentally studied by Liu et al. [9]. In addition, more experimental research on automotive coatings can be found in [10,11].

In consideration of experimental methods being of poor repeatability and high cost, numerical methods have become an attractive tool for investigating the impact problem. Many studies regarding the multi-particle impact test have been conducted [12–15]. With regard to the single-impact test, Toi et al. [16,17] established an elasto-viscoplastic-damage constitutive model and evaluated the impact resistance of automotive coatings in combination with a non-coupled analysis method. The mechanisms of impact energy absorption of a polymer coating had been numerically analyzed by Grujicic et al. [18]. Based on the stress field of the coating, Zhang et al. [19] investigated the spalling mechanism of polymer coating material under collision conditions. Furthermore, Xu et al. [20] carried out a debonding analysis of an organic coating–substrate structure under single impact with the help of a GPU parallel computational framework. In addition, the effect of coating thickness on the impact failure was analyzed as well, where the polymer-ply failure of the coating was simulated using the element deletion method [21]. To avoid the problem of mesh distortion and tangling existing in the traditional finite element method, Gong Yi et al. [22] utilized a coupled finite element and meshfree method to investigate the impact issue on a ductile metal pipe with a polymer coating. More relevant research can be found in [23–28]. However, the above studies cannot simultaneously reproduce the polymer-ply and interlaminar failures of the coating, which is not conducive to clarifying the impact failure mechanism of the polymer coating. In light of this, Zou et al. [29] proposed a computational framework for impact damage of polymer coatings, which accounts for both polymer-ply and interlaminar failures of the coating, and this method is verified by a single-impact simulation of a single-layered polymer coating. In summary, most existing numerical studies on the impact failure behavior are for single-layered polymer coatings. As for multi-layered polymer coatings, i.e., automotive coatings, there is still a lack of an effective finite element model to simulate the impact event.

Some theories have been proposed to explain the impact failure behavior of polymer coatings. It is reported that a polymer coating can fail in a brittle manner [30,31] or a ductile one [32,33]. In some cases, a transition between these two mechanisms can be observed. Ramamurthy et al. [34] attributed all the impact failure patterns to a tensile failure caused by dynamic effects. They argued that when stress waves propagate through the coating, local stress will exceed the yield strength of the material, which leads to fracture and interfacial delamination of the coating. Papini et al. believed that the impact failure mechanisms of the coatings with a strong interface and a weak interface are different, with the former dominated by toughness erosion [33] and the latter by quasi-static interfacial shear stress [35]. Zouari et al. [28] concluded that coating delamination is the result of three phenomena: Firstly, damage initiates at the interface due to shear stress. Then, radial compressive stress-driven coating buckling in turn exacerbates its debonding. Finally, the delamination propagates in mixed mode. The latest research shows that both brittle and ductile failures are found in the coating, and the interlaminar failure originates from interfacial shear stress and then propagates due to the coating buckling [29,36]. As mentioned above, the impact failure mechanisms of polymer coatings are complex, especially multi-layered polymer coatings, such as automotive coatings, whose properties of four paint films are different, and its impact failure mechanisms need to be further studied.

It is reported that primer plays an important role in the impact resistance of automotive coatings [37,38], and studies in this respect have been carried out. Through single-impact tests, Lonyuk et al. [39] revealed that a low glass transition temperature of the primer contributes to the better impact resistance of automotive coating systems. Another experimental study suggests that the crosslinker content of primer can also significantly affect the anti-impact performance of automotive coatings [40]. However, to the best of the authors' knowledge, the role of primer in the impact resistance of automotive coatings still lacks effective computational verifications.

In this paper, based on the computational framework developed by Zou et al. [29], a finite element model is developed to simulate the single-impact failure of automotive coatings. In this model, a multi-mechanism damage model and a large deformation cohesive zone model are employed to account for the polymer-ply and interlaminar failures of the coating, and some rate-dependent material models are adopted to capture the effect of impact velocity. With the help of this model, the impact failure mechanisms of the coating are numerically revealed. Finally, some parameter studies are conducted to investigate the influences of primer mechanical properties on the impact resistance of automotive coatings. It should be noted that a similar model can be found in a conference paper [41] by the author, and this paper builds on the previous work and studies a different impact condition. The main novelties of this paper can be summarized as follows:

1. A finite element model for single-impact failure of automotive coatings is developed, which accounts for not only the polymer-ply and interlaminar failures of the coating system but also the effect of impact velocity. The numerical results indicate that the proposed model can reproduce the failure patterns of automotive coatings and qualitatively capture the effect of impact velocity.
2. The impact failure mechanisms of automotive coatings are numerically revealed, the results show that both brittle and ductile failures are found in the coating, and there are three stages for the propagation of the delamination crack.
3. The effects of primer mechanical properties, i.e., Young's modulus, yield strength, and re-hardening modulus, on the impact resistance of automotive coatings are firstly numerically investigated.

The outline of this paper is as follows. Section 2 introduces the single-impact tests and the finite element model. Then, the experimental and numerical results are shown in Section 3, and the impact failure mechanisms of automotive coatings are also investigated. In Section 4, the effects of primer mechanical properties on the impact resistance of automotive coatings are numerically studied. Finally, a conclusion is drawn in Section 5.

2. Experiment and Modeling Descriptions

2.1. Experimental Procedure

A single-impact test on an automotive coating sample was conducted using a multifunctional anti-impact tester [9]. As shown in Figure 1, the sample consists of a metal substrate and four paint films, i.e., clearcoat, basecoat, primer, and electrocoat, whose in-plane size is 200 mm × 90 mm. The metal substrate is pretreated with zinc phosphate prior to painting. Except for the electrocoat, which is first electroplated on the metal substrate, other paint films are quantitatively sprayed by the ABB spraying robot in a specific order. In addition, each paint film is baked in strict accordance with the time and temperature specified by the manufacturer. Table 1 gives the thickness, main ingredient, and preparation process of each part of the sample. In this test, the long edge of the sample was clamped using a fixture, and a 2 mm diameter steel particle driven by a gas gun normally impacted the coating's center at 91.2 m/s.

Additionally, the chemical composition of each paint film is obtained with the help of a scanning electron microscope (SEM), and the results help to determine the failure patterns of the coating in the single-impact test.

To verify the ability of our finite element model to capture the effects of impact velocity, single-impact tests have been conducted with other impact velocities, i.e., 74 m/s, 83.3 m/s, 99.9 m/s, and 108.1 m/s. The damage degree of the coating is quantified with the radius of the delamination area. Each test is repeated three times to eliminate randomness, and the average delamination area radius is taken as the final result.
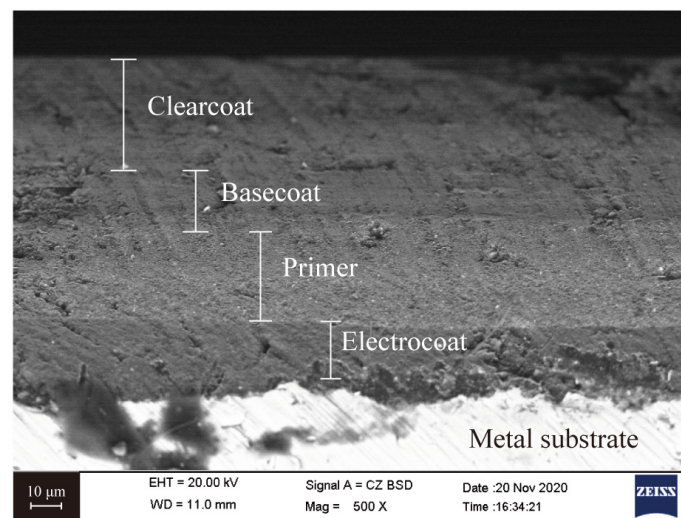
Figure 1. SEM photograph of the cross-section of the automotive coating sample.

Table 1. The thickness, main ingredient, and preparation process of each part of the automotive coating sample.

Part	Clearcoat	Basecoat	Primer	Electrocoat	Substrate
Thickness (mm)	0.0387	0.0229	0.0308	0.0199	0.850
Main ingredient	Solvent-based acrylic resin.	Waterborne acrylic resin.	Waterborne polyester resin.	Epoxy resin.	Cold rolled steel.
Preparation process	(1) Sprayed with ABB robot. (2) Let it sit for 7 min. (3) Baked at 140 °C for 30 min.	(1) Sprayed with ABB robot. (2) Pre-dried at 80 °C for 5 min. (3) Cooled down to room temperature.	(1) Sprayed with ABB robot. (2) Pre-dried at 80 °C for 5 min. (3) Baked at 150 °C for 30 min.	(1) Electrophoresis process. (2) Cleaned with ionic water. (3) Baked at 150 °C for 30 min.	-

2.2. Finite Element Model

2.2.1. Coating Failure Model

In this finite element model, the coatings' mechanical behavior is simulated using a strain-rate-dependent piecewise linear elastic-plastic model, which is introduced in Section 2.2.3. In addition, it is believed that automotive coatings can fail in a brittle or ductile manner. In light of this, a multi-mechanism damage model accounting for these two damages is employed to simulate the polymer-ply failure of the coating, and the Cauchy stress tensor is calculated by:

$$\boldsymbol{\sigma} = (1 - D)\boldsymbol{\sigma}_{\text{eff}} \tag{1}$$

$$D = 1 - (1 - d_1)(1 - d_2) \tag{2}$$

where D is the overall damage variable. D is initially equal to 0, which means the material is intact, and $D = 1$ indicates that the material fails. Considering that the element deletion may lead to unphysical failure patterns under compression, the upper limit of D is set to 0.95 in this model in the absence of element erosion. Such treatment can be found in the work by Nguyen et al. [42]. $\boldsymbol{\sigma}_{\text{eff}}$ is the effective (undamaged) stress tensor; d_1 and d_2 are brittle and ductile damage variables, respectively. To ease softening-induced mesh size sensitivity, a crack band [43,44] method is used in this work.

The onset of brittle damage is defined by the maximum tensile stress failure criterion, and the brittle damage variable d_1 is given by:

$$d_1 = \max\left[0, \min\left(1, \frac{\varepsilon_{\text{eff,f}}(\varepsilon_{\text{eff,max}} - \varepsilon_{\text{eff,0}})}{\varepsilon_{\text{eff,max}}(\varepsilon_{\text{eff,f}} - \varepsilon_{\text{eff,0}})}\right)\right] \tag{3}$$

where $\varepsilon_{\text{eff,f}}$ denotes the ultimate effective strain; $\varepsilon_{\text{eff,max}}$ is the maximum effective strain accounting for damage irreversibility; $\varepsilon_{\text{eff,0}}$ represents the effective strain at damage initiation. In addition, the critical energy release rate $G_{\text{c,1}}$ for brittle damage is calculated by:

$$G_{\text{c,1}} = \frac{1}{2}\sigma_{\text{t}}(\varepsilon_{\text{eff,f}} - \varepsilon_{\text{eff,0}})L_{\text{e,d}} \tag{4}$$

where σ_{t} is the tensile strength, and $L_{\text{e,d}}$ is the characteristic length of the element. The effective strain in Equations (3) and (4) is the Rankine equivalent strain [43], expressed as:

$$\varepsilon_{\text{eff}} = \frac{1}{E}\max_{i=1,2,3}\sigma_{\text{eff},i} \tag{5}$$

where E is Young's modulus, and $\sigma_{\text{eff},i}$, $i = 1,2,3$ are principal effective stresses.

An effective plastic strain-based criterion is employed to model the damage onset of ductile failure. It is assumed that the evolution of ductile damage variable d_2 is governed by the following law:

$$d_2 = \begin{cases} 0 & \varepsilon_{\text{p}} < \varepsilon_{\text{p,c}} \\ \int \frac{L_{\text{e,d}}}{u_{\text{p,f}}}\text{d}\varepsilon_{\text{p}} & \varepsilon_{\text{p}} \geq \varepsilon_{\text{p,c}} \end{cases} \tag{6}$$

$$u_{\text{p,f}} = \frac{2G_{\text{c,2}}}{\sigma_{\text{y0}}} \tag{7}$$

where $\varepsilon_{\text{p,c}}$ is the critical effective plastic strain; $G_{\text{c,2}}$ is the critical energy release rate for ductile failure; σ_{y0} is the von Mises effective stress when failure criterion is reached. Both characteristic lengths of these two mechanisms are calculated by the approach of Skamnioties et al. [44].

After damage initiation, the elements are susceptible to distortion under compression loading when calculating with Equation (1), and a so-called microdefects closure technique [45] is adopted to deal with it. Equation (1) is reformulated as:

$$\boldsymbol{\sigma}_{\text{eff}} = \frac{1}{1-D}\boldsymbol{\sigma}^+ + \frac{1}{1-HD}\boldsymbol{\sigma}^- \tag{8}$$

$$\boldsymbol{\sigma}^+ = \sum_i \langle\sigma_i\rangle(\boldsymbol{e}_i \otimes \boldsymbol{e}_i), \; \boldsymbol{\sigma}^- = \boldsymbol{\sigma} - \boldsymbol{\sigma}^+ \tag{9}$$

where H is a material-dependent microdefects closure parameter, and typically $H = 0.2$. $\boldsymbol{e}_i$, $i = 1, 2, 3$, are the principal axes of the Cauchy stress tensor $\boldsymbol{\sigma}$. $\langle\cdot\rangle$ is the Macaulay bracket defined as $\langle x\rangle = \max(x,0)$.

Parameters of the damage model are given in Table 2. The tensile strengths of the paint films are chosen as relatively higher values, and these selections are based on the following considerations. Firstly, it is widely accepted that the tensile strengths of the polymer materials are positively correlated with the strain rate [46,47], and the tensile strength can reach as high as 200 MPa at 3800 s^{-1} [47]. Secondly, impact loadings can bring in extremely high strain rates of the coating, e.g., millions per second. Therefore, during the impact process, the paint films' tensile strengths are likely to be within this range.

Table 2. Parameters of the damage model.

Paint Film	σ_{t} (MPa)	$\varepsilon_{\text{p,c}}$	$G_{\text{c,1}}$ (N/m)	$G_{\text{c,2}}$ (N/m)
Clearcoat	400	1.3	290	15
Basecoat	310	1.06	85	16
Primer	330	0.92	180	13
Electrocoat	350	1.23	220	10

It needs to be declared that since each paint film is of micron thickness and the strain rate is extremely high (about 10^6 s^{-1}), it is difficult to obtain reliable damage parameters through experimental methods. According to the authors' review of the literature, there

are no reliable damage parameters for reference in the published literature. In light of this, in this model, the damage parameters are adjusted by comparing the simulation phenomenon with the experimental one. In the future, the development of a reliable parameter identification method is an essential step to make it a model of higher fidelity.

2.2.2. Large Deformation Cohesive Zone Model

The experimental results show that there is no interlaminar failure in the paint film's interfaces, and delamination occurs in the interface between the coating and substrate. In light of this, the interfaces between the paint films are seen as perfect in this model, and only the interlaminar failure between the electrocoat and the substrate is considered. Since a numerical problem may take place when a commonly used cohesive element is employed in this large deformation situation [36], a contact/cohesive-type large deformation cohesive zone model (LDCZM) is developed to ensure the stable calculation of coating delamination under mixed-mode loading. This method enables the use of non-matching meshes, which introduces additional freedom in discretization. In addition, in an impact failure simulation of a single-layered polymer coating, LDCZM produced a smoother stress distribution and exhibited better convergency than the widely used intrinsic cohesive zone model [36].

In the LDCZM, the total mixed-mode relative displacement δ_m is defined as:

$$\delta_m = \sqrt{\langle \delta_n \rangle^2 + \delta_t^2} \tag{10}$$

where δ_n, δ_t are the normal and tangential relative displacement, with $\delta_t = |\boldsymbol{\delta}_t|$, $\boldsymbol{\delta}_t$ being the tangential relative displacement vector, which is updated incrementally.

For mixed-mode damage initiation, a quadratic stress criterion is adopted, which is written as:

$$\left(\frac{\langle T_n \rangle}{N} \right)^2 + \left(\frac{T_t}{S} \right)^2 = 1 \tag{11}$$

where N and S are tensile and shear strengths whose values are set to 15.5 MPa [48] in this work. Therefore, the effective damage initiation relative displacement is calculated through:

$$\delta_0 = \begin{cases} \delta_{n,0} \delta_{t,0} \sqrt{\frac{1+\beta^2}{\delta_{t,0}^2 + \beta^2 \delta_{n,0}^2}} & \delta_n > 0 \\ \delta_{t,0} & \delta_n \leq 0 \end{cases} \tag{12}$$

$$\beta = \left\langle \frac{\delta_t}{\delta_n} \right\rangle \tag{13}$$

where $\delta_{n,0} = N/K$, $\delta_{t,0} = S/K$ are the damage initiation relative displacements in pure tensile and shear modes, with K being the interfacial stiffness.

The propagation of mixed-mode damage is described by a power law given by:

$$\left(\frac{G_n}{G_{nc}} \right)^\kappa + \left(\frac{G_s}{G_{sc}} \right)^\kappa = 1 \tag{14}$$

where G_n and G_s are the energy release rates for mode I and mode II; G_{nc} and G_{sc} denote the critical energy release rates for mode I and mode II, and here we set $G_{nc} = G_{sc} = 150$ N/m [49]; κ is a parameter. Then, the ultimate mixed-mode relative displacement is:

$$\delta_f = \begin{cases} \frac{2(1+\beta^2)}{K\delta_0} \left[\frac{1}{G_{nc}^\kappa} + \left(\frac{\beta^2}{G_{sc}} \right)^\kappa \right]^{-\frac{1}{\kappa}} & \delta_n > 0 \\ \delta_{t,f} & \delta_n \leq 0 \end{cases} \tag{15}$$

where $\delta_{t,f} = 2G_{sc}/S$ is the ultimate relative displacement in mode II.

It is reported that friction in the damaged area plays a major part in increasing the resistance to model II failure under compression loading [50]. To account for friction effects,

Coulomb's friction law is incorporated into the employed LDCZM. So, the normal and tangential traction components are expressed as:

$$T_{\mathrm{n}} = (1 - d)K\delta_{\mathrm{n}} - dK\langle -\delta_{\mathrm{n}} \rangle \tag{16}$$

$$\boldsymbol{T}_t = (1 - d)K\boldsymbol{\delta}_t + \boldsymbol{T}_{\mathrm{t,f}} \tag{17}$$

where the damage variable d is initially equal to 0, and it evolves the Kuhn–Tucker condition; $\boldsymbol{T}_{\mathrm{t,f}}$ denotes the friction stress on the damaged part of the interface, and it is given by:

$$\boldsymbol{T}_{\mathrm{t,f}} = d\boldsymbol{\sigma}_{\mathrm{t,coh}} \tag{18}$$

in which $\boldsymbol{\sigma}_{\mathrm{t,coh}}$ is calculated based on Coulomb's friction law, so a friction coefficient is needed, and we set it to 0.5.

Finally, the LDCZM is integrated with an element-based mortar algorithm [51,52].

2.2.3. Simulation Configuration

The simulation configuration of impact failure of automotive coatings is shown in Figure 2. The model is composed of a substrate, a multi-layered coating, and a particle. It should be emphasized that the multi-layered coating contains four paint films, i.e., the clearcoat, basecoat, primer, and electrocoat. Additionally, the dimensions of each part are consistent with those in the experiment. The particle has an initial velocity of 91.2 m/s, and the physical time of this simulation is selected as 40 μs to ensure that the whole failure process of the coating can be captured. Thanks to symmetric conditions, one quarter of the model is taken for discretization with fully integrated 8-node hexahedron solid elements. Since the experimental results show that no interlaminar failure occurs at the interfaces between the paint films, these interfaces are simulated by sharing nodes. To minimize the computational cost without compromising the accuracy of the simulation, mesh transitions are adopted, and the coating in the vicinity of the impact location is discretized with a finer mesh with a minimum in-plane element dimension of 10 μm, which is determined by a mesh convergence analysis introduced in Section 3. It is worth noting that the employed LDCZM allows using non-matching meshes at the interface, and the substrate is not the interested component. Therefore, the coarser meshes are used to discretize the substrate for better computational efficiency. As for the boundary conditions, the translational degrees of freedom of nodes on two symmetry planes are restricted in the x-direction (U1 = 0) and y-direction (U2 = 0), respectively, and the nodes of the clamped area outside the model are subjected to fixed constraints (U1 = U2 = U3 = 0). In addition, a contact algorithm based on the element-based mortar algorithm is used to calculate the contact force between the particle and coating, and the friction coefficient is set to 0.3 [53]. In this model, the element numbers of the particle, coating, and substrate are 2088, 60,288, and 10,350.

The steel particle is assumed to behave in a linear elastic manner. A simplified Johnson–Cook model is employed to model the mechanical behavior of the substrate. In this simplified model, the effect of temperature is ignored, and the yield stress is calculated through the following equation:

$$\sigma_{\mathrm{y}} = \left(A + B\varepsilon_{\mathrm{p}}^{n} \right)\left(1 + C\ln\frac{\dot{\varepsilon}}{\dot{\varepsilon}_0} \right) \tag{19}$$

where A is the yield stress of zero plastic strain and unit plastic rate; B is the strain hardening constant; ε_{p} is the equivalent plastic strain; n is the strain hardening exponent; C is the strain-rate constant; $\dot{\varepsilon}$ is the strain rate; $\dot{\varepsilon}_0$ is the reference strain rate. The material parameters of the finite element model are presented in Table 3.
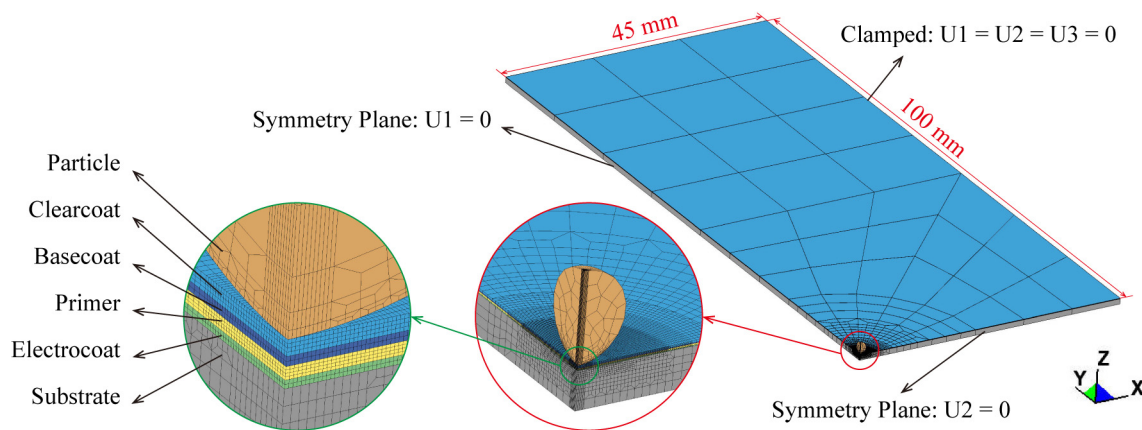
Figure 2. Meshes, main dimensions, and boundary conditions of the finite element model in the single-impact simulation of the automotive coating system. The particle has an initial impact velocity of 91.2 m/s.

Table 3. Material models and parameters of the finite element model.

| Part	Material Model	Parameters
Clearcoat	Strain-rate-dependent piecewise-linear-plastic model	ρ = 1325 kg/m^3, E = 8.1 GPa, v = 0.15, C_{CS} = 3.2476 ms^{-1}, P_{CS} = 10.2033
Basecoat	Strain-rate-dependent piecewise-linear-plastic model	ρ = 903 kg/m^3, E = 4.5 GPa, v = 0.15, C_{CS} = 1.558 ms^{-1}, P_{CS} = 7.7133
Primer	Strain-rate-dependent piecewise-linear-plastic model	ρ = 1663 kg/m^3, E = 3.2 GPa, v = 0.15, C_{CS} = 2.5461 $\times$ 10^{-6} ms^{-1}, P_{CS} = 17.392
Electrocoat	Strain-rate-dependent piecewise-linear-plastic model	ρ = 1435 kg/m^3, E = 2.96 GPa, v = 0.15, C_{CS} = 12.3505 ms^{-1}, P_{CS} = 2.8723
Particle [54,55]	Linear elastic model	ρ = 7860 kg/m^3, E = 199.6 GPa, v = 0.29
Substrate [49,56]	Johnson–Cook model	ρ = 7860 kg/m^3, E = 210 GPa, v = 0.29, A = 610 MPa, B = 425 MPa, C = 0.03, n = 0.547, $\dot{\varepsilon}_0$= 1.68 ms^{-1}

Automotive coatings are a typical polymer coating whose mechanical properties are highly nonlinear and usually exhibit strain-rate dependency. To accurately describe the response of the coating during the impact, its mechanical behavior is simulated using a piecewise-linear-plastic model based on the J2 flow criterion. It is worth noting that since the coatings suffer from large plastic deformation during impact events, the plastic stage of the material mechanical behavior is our focus. For simplicity, the viscoelastic properties of the polymer are disregarded, and the assumption of rate-independent elastic behavior is adopted in this material model. Additionally, the Cowper–Symonds model is used to account for the strain-rate-dependent effect, which is expressed as:

$$\sigma_{y,d} = \sigma_{y,s}(\varepsilon_p)\left[1 + \left(\frac{\dot{\varepsilon}}{C_{CS}}\right)^{\frac{1}{P_{CS}}}\right] \tag{20}$$

where $\sigma_{y,d}$ is the dynamic yield stress; $\sigma_{y,s}(\varepsilon_p)$ is given by a yield-stress-effective plastic strain curve; C_{CS} and P_{CS} are parameters. Four paint films' densities are measured using a DH-300 DahoMeter digital density meter [3]. The Young's moduli and yield-stress-effective plastic strain data of coating are identified from the high strain-rate compression experimental curves in the literature [57,58], as shown in Table 4. The parameters C_{CS} and P_{CS} are calibrated using the yield stress values at multiple strain rates, and a comparison between the experimental data and predicted stress–strain curves of these four paint films at different strain rates is given in Figure 3.

Table 4. The yield-stress-effective plastic strain data of each paint film.

Clearcoat		Basecoat		Primer		Electrocoat	
Effective Plastic Strain	Yield Stress (MPa)	Effective Plastic Strain	Yield Stress (MPa)	Effective Plastic Strain	Yield Stress (MPa)	Effective Plastic Strain	Yield Stress (MPa)
0.00008	37.2353	0	2.7105093	0.005724	20.60382	0	12.772
0.0055191	53.113362	0.000598	31.66019	0.024861	39.24316	0.0125	86.33883
0.0225235	66.738064	0.0179	47.805988	0.03502	43.01446	0.02835	100.1326
0.120563	77.49831	0.0418	57.72799	0.061612	47.30946	0.04835	102.6869
0.1519405	79.43251	0.0852	69.904982	0.113637	50.54532	0.221	78.15169
0.21885	89.99594	0.119	72.61098	0.18513	67.48708	0.315	81.70818
-	-	0.171	80.72898	-	-	0.4285	97.575623
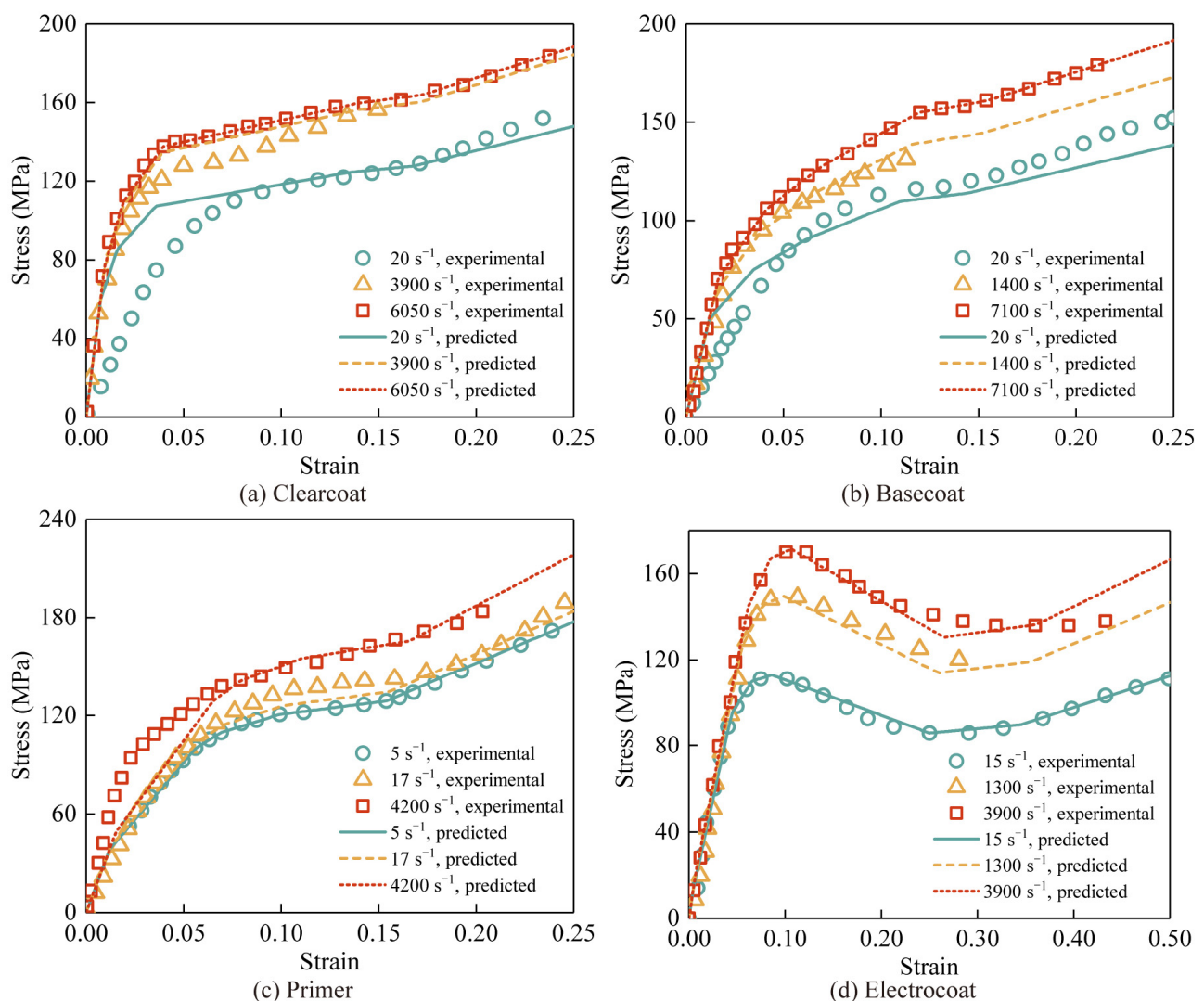
Figure 3. Comparison between experiment data [57,58] and predicted stress–strain curves of four paint films, i.e., (**a**) clearcoat, (**b**) basecoat, (**c**) primer, and (**d**) electrocoat, at different strain rates.

3. Results and Discussion

3.1. Experimental Results

Figure 4 shows the results of the single-impact experiment on automotive coatings. As can be seen in Figure 4a, there exists a crater centered on the impact point. In addition, coating buckling is found at the edge of the crater, which indicates the occurrence of

delamination. It is measured that the radius of the delamination area is about 1.43 mm. The failure patterns of coating observed using SEM are presented in Figure 4b. Material removal can be observed at a circular damaged region (marked with a red dotted circle) near the impact point, which results in the exposures of two bottom layers, with one within the smaller yellow dotted circle and the other located between both circles. What is more, there are multiple radial cracks that are distributed on the periphery of the central damaged region.

(a)   (b)
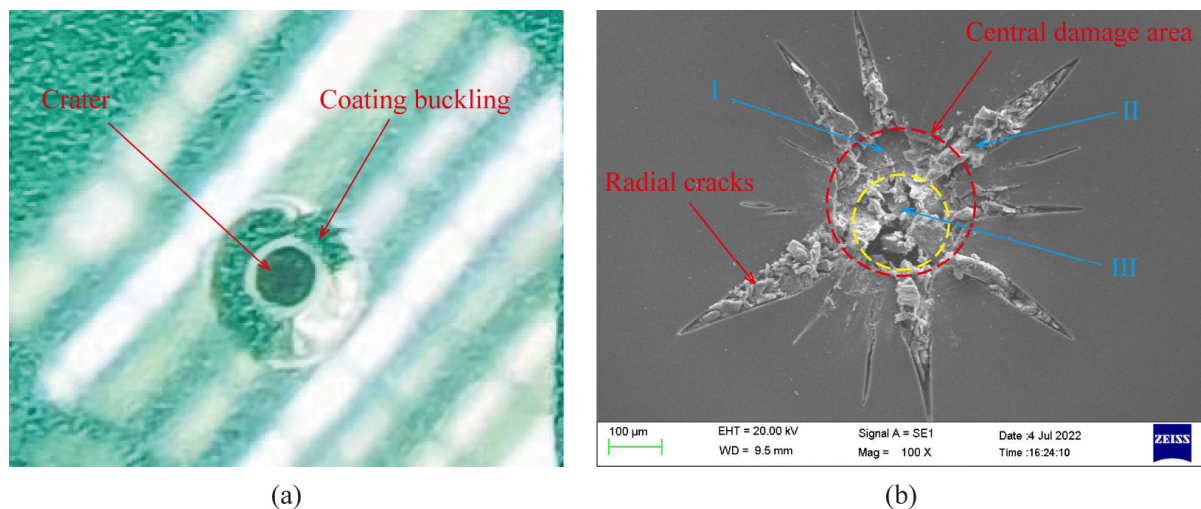
Figure 4. (**a**) The appearance of the sample after impacting. (**b**) SEM photograph of the sample.

The chemical compositions of each paint film determined by SEM are listed in Table 5. As shown in Table 5, there is no Ti in the clearcoat and basecoat, and the Ti concentration of the primer is orders of magnitude different from the ones of Al and Si, while the concentrations of Ti, Al, and Si of the electrocoat are close. For a better understanding of the coatings' failure patterns, the same treatment is adopted to obtain the chemical compositions of materials in regions I, II, and III (see Figure 4b), and the results are presented in Table 6. According to Table 6, regions I and II contain Ti, and its concentration is orders of magnitude different from the ones of Al and Si. So, it can be concluded that the exposed film in region I within the central damaged area is the primer, which means that the central damaged areas of clearcoat and basecoat are larger than the one of primer. In addition, the material below the radial crack in region II also belongs to the primer, indicating that radial cracks went through the clearcoat and basecoat and reached the primer. Furthermore, the concentrations of Ti, Al, and Si in region III are close, and the material in region III is determined to be electrocoat, which suggests that the central damage propagated to the electrocoat, and no delamination occurs at the interface between the paint films. In other words, interlaminar failure occurs at the interface between the coating and the substrate.

**Table 5.** Chemical compositions of each paint film determined by SEM.

Elements (at.%)	Clearcoat	Basecoat	Primer	Electrocoat
C	74.89	77.11	57.38	70.84
O	24.92	19.05	33.64	23.90
Ti	-	-	6.63	1.58
Al	0.19	3.11	0.23	1.74
Si	-	-	0.95	1.59
Others	-	0.73	1.17	0.35

Table 6. Chemical compositions of materials in regions I, II, and III in Figure 4b, determined by SEM.

Elements (at.%)	Region I	Region II	Region III
C	38.68	54.11	63.68
O	19.63	28.89	28.50
Ti	37.47	14.54	4.28
Al	0.46	0.69	1.42
Si	1.41	0.73	1.55
Others	2.35	1.04	0.57

3.2. Simulation Results

A mesh convergence analysis was performed to ensure a sufficient mesh density for accurately capturing the deformation process. In this analysis, the minimum in-plane sizes of coating elements are chosen as 10 μm, 15 μm, and 20 μm, and the thickness direction dimension is close to the in-plane dimension. A refinement zone centered on the impact point is divided for the substrate, with a radius of 0.6 mm and a depth of 0.24 mm. The in-plane size of elements within this domain is the same as the coating elements close to the impact point. Results simulated using these three meshes are presented in Figure 5 and Table 7. As can be seen, the impact force histories simulated using these three meshes show a high degree of consistency. Taking the prediction corresponding to element size of 10 μm as the exact solution, the maximum error in delamination area size is only 0.54%, which suggests that the adopted element sizes are small enough to achieve a convergent solution. Based on the analysis above, we selected a mesh with the minimum element size of 10 μm to discrete the coating, because we are interested in the coating failure. Additionally, thanks to the LDCZM employed, a coarser mesh is chosen for the substrate. The size of the substrate mesh is almost twice the one of the coating mesh in the vicinity of the impact center, and its minimum element size is about 20 μm. The results simulated using the final mesh are shown in Figure 5 and Table 7. As shown, the final mesh helps to obtain results with acceptable precision at a small numerical cost.
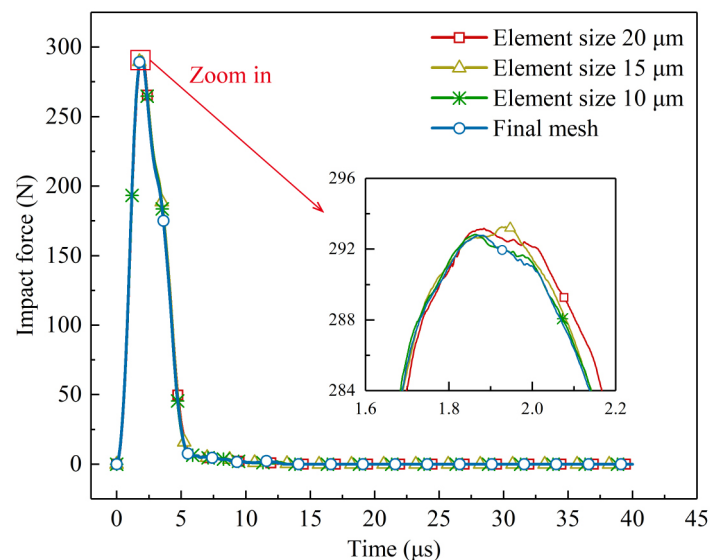
Figure 5. Impact force histories simulated using different meshes.

Table 7. Predicted delamination area sizes using different meshes.

Mesh	20 μm	15 μm	10 μm	Final Mesh
Delamination area radius (mm)	1.49654	1.48854	1.49657	1.41735

Due to the complex clamping conditions in the experiment, a fixed constraint boundary condition is adopted in the simulation model for simplification. To determine the influence of boundary conditions on the simulation results, various boundary conditions on the long edge of the sample are also taken into consideration with the final mesh, i.e., free, pinned, sliding, and fixed, as shown in Figure 6. Except for the investigated conditions, parameters remain the same as those presented in Section 2. The predicted outcomes of these four boundary conditions are given in Figure 7 and Table 8. As can be observed, the impact force histories are indistinguishable from each other. On the other hand, compared to the fixed condition, the others produce a maximum relative error of around 1.34% in terms of delamination area radius. Hence, when the in-plane size of the specimen is large enough, the boundary condition has little effect on the impact response of automotive coatings due to damage localization.
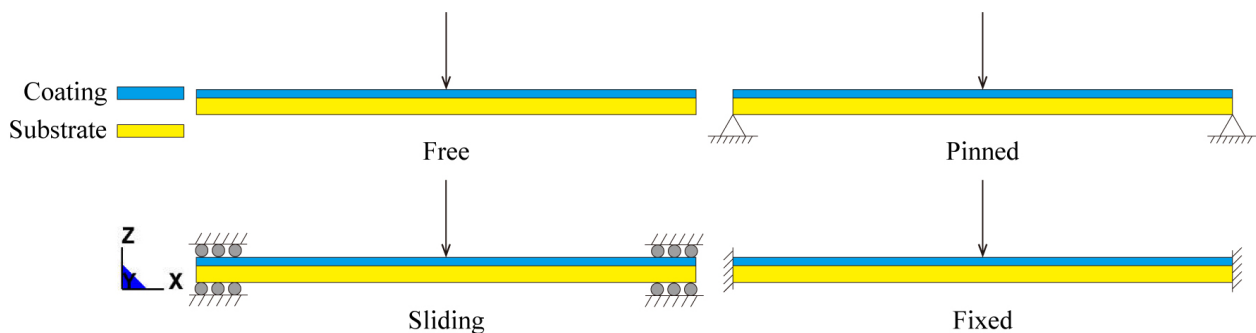
Figure 6. Boundary conditions.
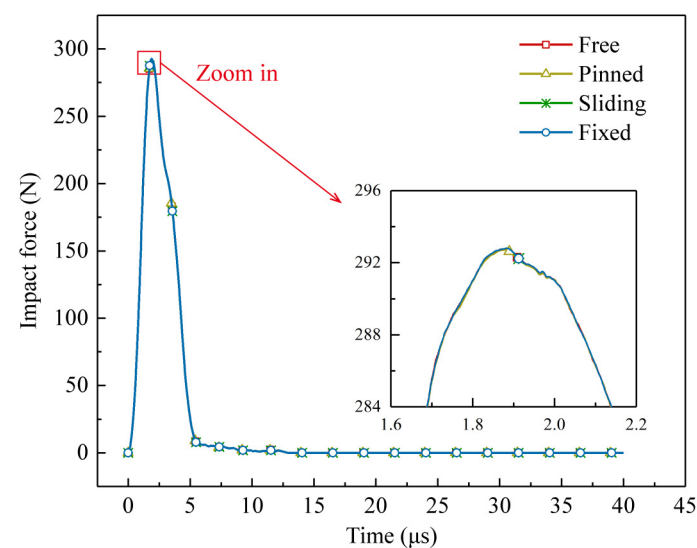
Figure 7. Impact force histories simulated using different boundary conditions with final mesh.

Table 8. Predicted delamination area sizes using different boundary conditions with final mesh.

Boundary Condition	Free	Pinned	Sliding	Fixed
Delamination area radius (mm)	1.43639	1.43640	1.43638	1.41735

Figure 8 shows a comparison between the experimental and simulated polymer-ply damage patterns. It is important to note that the elements with overall damage value *D* in the range of 0.949–0.95 are considered to be completely failed, and here we remove them using the postprocessing software so that the predicted damage phenomenon can be observed more clearly. In addition, if all elements around an area are completely failed,

it is believed that the coating material in this area is separated from the sample in the form of fragments, so the elements in this area are also removed. Finally, the numeric results are presented in a half-model manner through reflection. The reflection and removal operations will also be used in the subsequent demonstration of simulation phenomena. As displayed in Figure 8, the simulation reproduces the central damaged region and radial cracks in the single-impact test. It is noteworthy that the simulated crack pattern has differences from the experimental one, such as the size and the number of cracks. However, as one of the earliest simulation studies on automotive coating impact failure, our goal is to build a viable model that can qualitatively capture the crack patterns. In this sense, these discrepancies are acceptable. On the other hand, Figure 9 presents the numerical interlaminar failure between the coating and the substrate. The simulated delamination area radius is 1.41735 mm, and the relative error to the experimental value of 1.43 mm is only 0.88%. Consequently, the competence of the coating impact finite element model in qualitatively simulating the polymer-ply failure patterns and quantitatively predicting the delamination area has been verified.
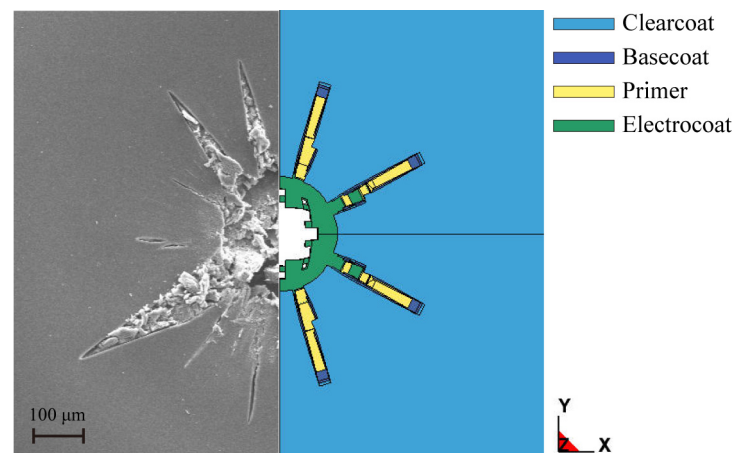
Figure 8. A comparison between the experimental (left) and simulated (right) polymer-ply damage patterns. The area displayed is a part of the finite element model.
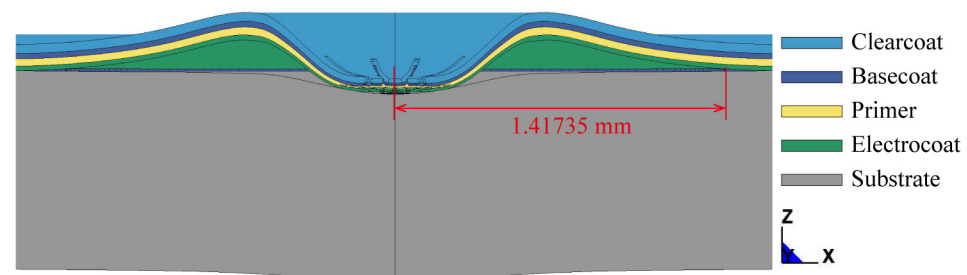
Figure 9. The predicted delamination area between coating and substrate. The model shown has been reflected in *Y-Z* plane.

To have a more intuitive understanding of the in-ply failures, the predicted polymer-ply failure patterns of four paint films are displayed in Figure 10. It is worth noting that the range of legend values for the contour plot is set as 0.949–0.95 without interpolation of the damage variable, so the elements in red are considered to be completely failed. As can be seen, a circumferential crack and radial cracks can be found in the clearcoat. Both the central damage and radial cracks are observed in the basecoat. For the two bottom paint films, only central damage occurs. It is interesting that although elements in region A have not been fully damaged, a circumferential crack has gone around this region. So, it is believed that the coating material in this region is removed from the sample in the form of a fragment.
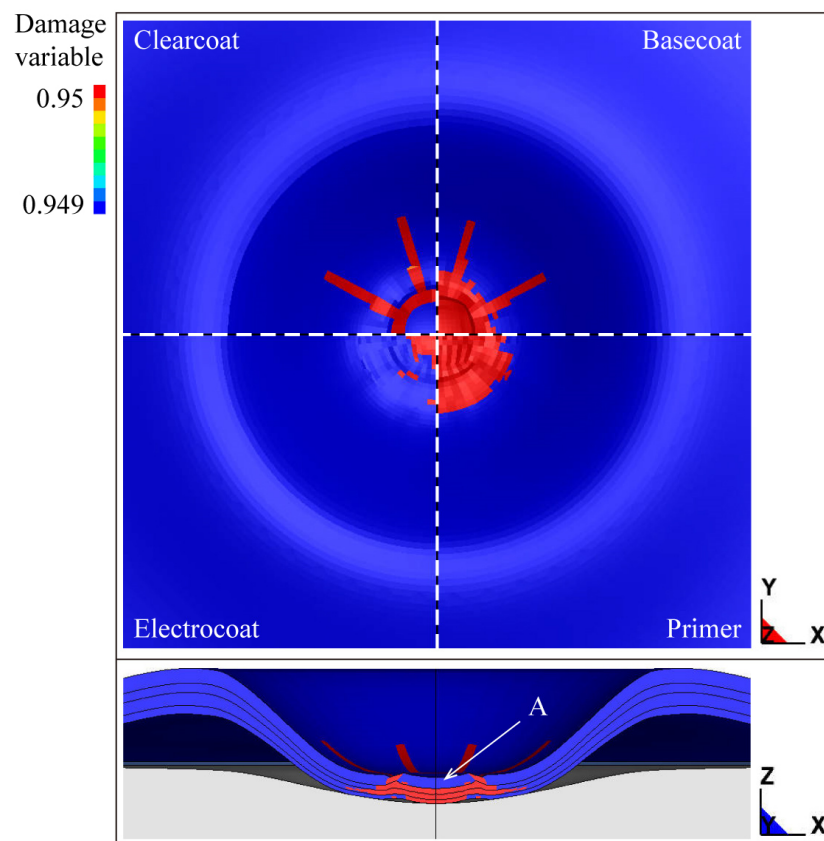
Figure 10. The predicted polymer-ply failure patterns of four paint films.

Figures 11 and 12, respectively, present the evolutions of polymer-ply and interlaminar failures of the coating. As can be seen at the moment of 0 μs, the particle impacts the coating and moves downward. As the particle squeezes the coating, at 0.52 μs, a significant relative tangential displacement is observed at the coating–substrate interface, which suggests that the onset of interlaminar failure is caused by interface shear stress. Then, damage initiation occurs in the primer at about 1.24 μs. At this moment, as demonstrated in Figure 13a, the negative maximum principal stresses distributed in this region do not meet the failure criterion of brittle damage, whereas the effective plastic strain in this area is high enough and has exceeded the corresponding critical value. Hence, a ductile failure of the primer is triggered. Later, as the particle continues to extrude, the damaged area rapidly propagates along the radial and thickness directions.

When the time comes to 4.08 μs, the particle reaches the lowest point, and then it rebounds upward. Since the pressure and friction force on the coating start decreasing, radial compressive stress causes the coating material under the impact point to flow outwards, resulting in coating buckling, and hence the delamination crack extends both outwards and inwards. At the same time, the outward flow of the coating material promotes plastic deformation of the coating, giving rise to the central damages of the basecoat and electrocoat at 4.28 μs and 4.76 μs, and the corresponding contours of maximum principal stress and effective plastic strain are, respectively, depicted in Figure 13b,c. Similar to the primer, these two paint films fail in a ductile manner. Then, the particle continues to move backward, and the plastic deformation of the coating keeps growing. Consequently, the damage of the lower three layers of coating further expands until these paint films completely failed.
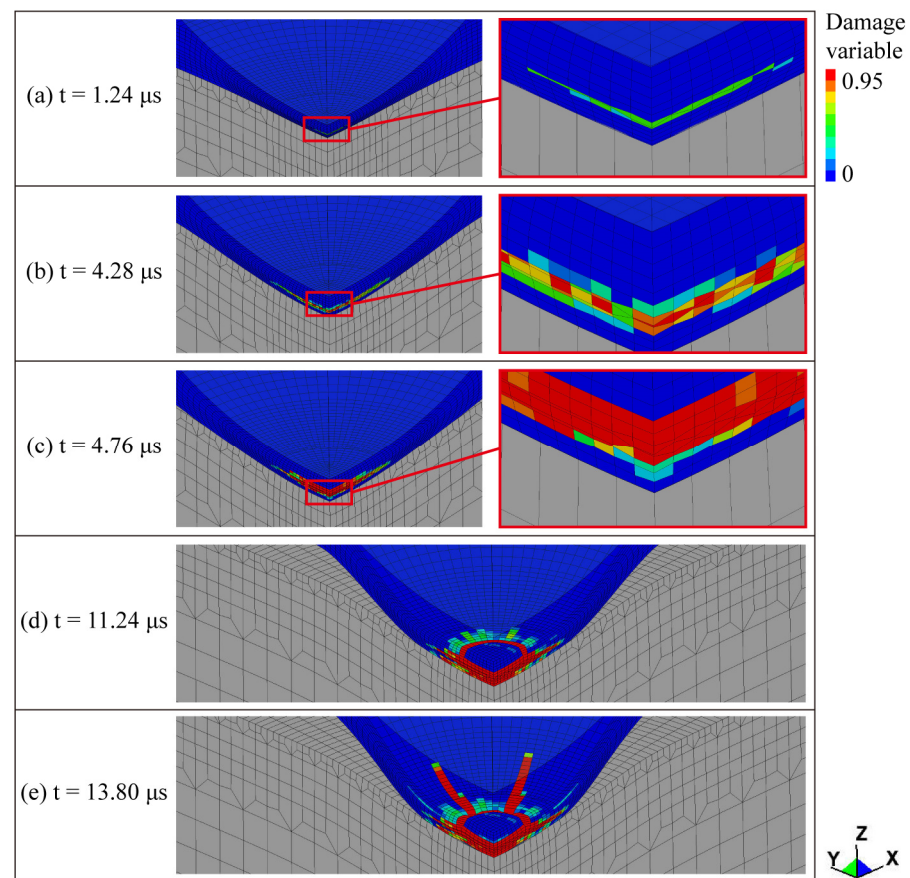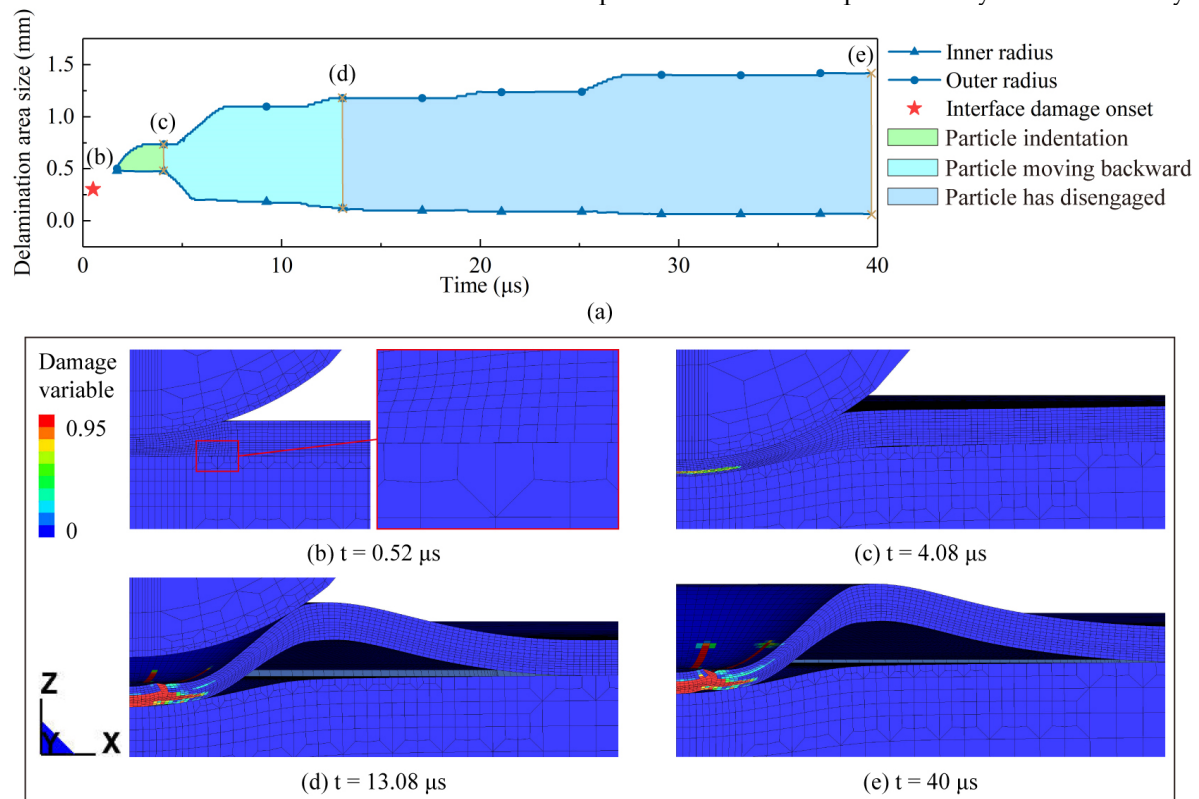
Figure 11. Polymer-ply damage evolution of automotive coatings. (**a**) 1.24 μs, damage initiation occurs in the primer. (**b**) 4.28 μs, the central damage of the basecoat appears. (**c**) 4.76 μs, the central damage of the electrocoat occurs. (**d**) 11.24 μs, a circumferential crack appears in the clearcoat. (**e**) 13.80 μs, the radial cracks occur in the clearcoat and finally extend to the basecoat. The contour plot is displayed without interpolation of the damage variable.

On the other hand, as the particle moves backward, outward coating material flow increases the radial tensile stresses near the impact center, which brings about a circumferential crack in the clearcoat at around 11.24 μs. Subsequently, the coating material outside this crack further flows outward, increasing the circumferential tensile stresses in the area that is slightly far away from the impact site, as shown in Figure 14. As a result, radial cracks appear. After that, these cracks propagate along the radial and thickness direction and finally extend to the basecoat at 13.8 μs. At the same time, the outflow of coating material also intensifies coating buckling and interlaminar failure. Until 13.08 μs, the particle disengages from the coating. Then, the coating vibrates at different frequencies from the substrate due to the stress wave, which leads to the further extension of the delamination. Finally, at 40 μs, the outer radius of the delamination region reaches 1.41735 mm, and it is close to the experimental counterpart.

To verify the capacity of this finite model in capturing the effect of impact velocity, the impact behaviors of automotive coatings are simulated with different impact velocities, i.e., 74 m/s, 83.3 m/s, 91.2 m/s, 99.9 m/s, and 108.1 m/s. The predicted results are shown in Figure 15. As can be seen, since a higher impact velocity means that the coating is subjected to a greater loading, the outflow of the coating material is intensified. As a result, the delamination area size is positively correlated with the impact velocity, which is consistent with the experimental outcome. However, in the range of 74~91 m/s, the predicted trend is quite different from the experimental one, which may be attributed to many factors, such as the absence of rate-dependent damage models, the rate-independent assumption of automotive coating elastic behavior, and the effects of the rate-independent cohesive zone

model. Finally, we conclude that the rate-dependent material model is somewhat helpful in considering the effects of impact velocity, but some improvements are still needed for the finite element model to capture the effect of impact velocity more accurately.


Figure 12. Interlaminar failure evolution of automotive coatings. (**a**) Histories of delamination area sizes. (**b–e**) Damage evolution: (**b**) 0.52 μs, delamination onset. (**c**) 4.08 μs, the particle reaches the lowest point. (**d**) 13.08 μs, the particle disengages from the coating. (**e**) 40 μs, the final state of interlaminar failure. The contour plot is displayed without interpolation of the damage variable.
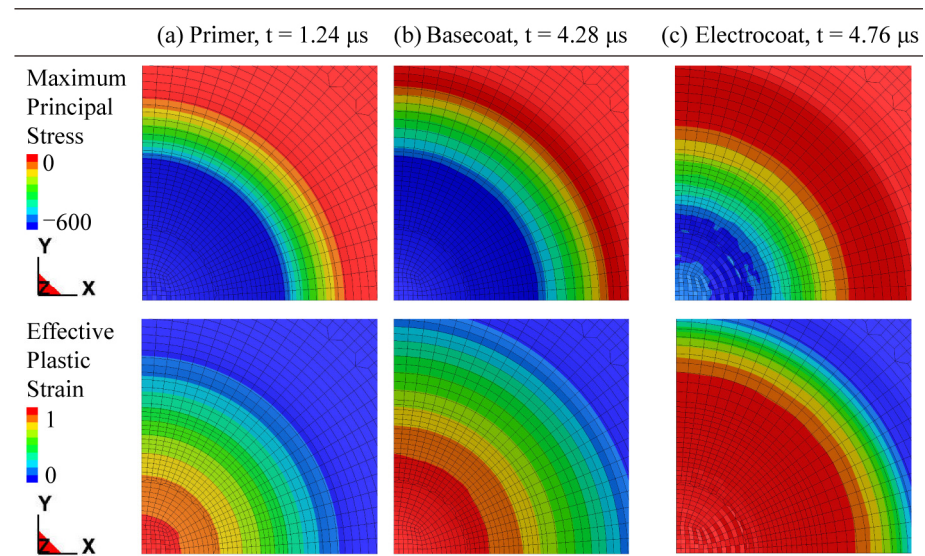
Figure 13. Distributions of maximum principal stress and effective plastic strain of (**a**) primer at 1.24 μs, (**b**) basecoat at 4.28 μs, and (**c**) electrocoat at 4.76 μs in the vicinity of the impact location.
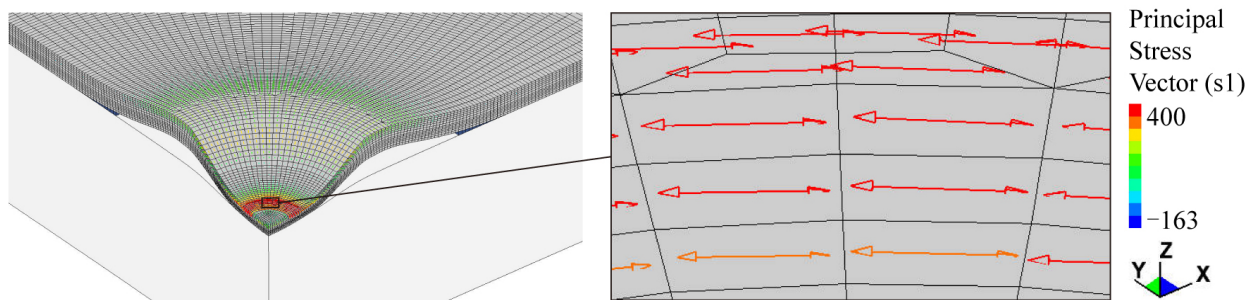
Figure 14. Vector of the maximum principal stress of clearcoat at 11.56 µs.
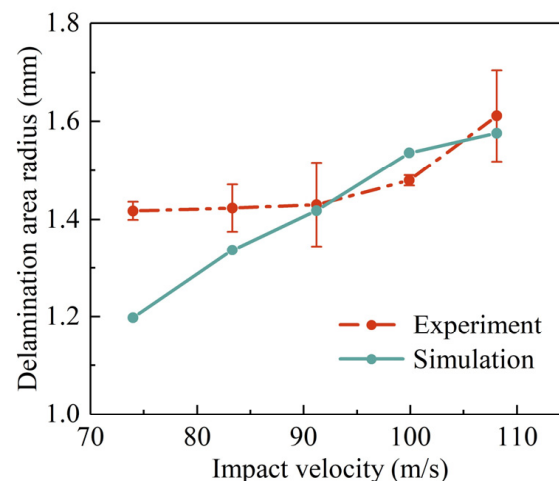
**Figure 15.** Experimental and predicted delamination area radius with different impact velocities.

4. Parametric Studies

In this section, with the help of the finite element model built in Section 2, the influences of primer mechanical properties on the impact resistance of automotive coatings are investigated, and the primer mechanical properties include Young's modulus and yield behavior. It needs to be emphasized that in this section, except for the parameters studied, the others are consistent with those in Section 2. Since the single impact does not lead to a large, damaged area of the coating, only a local region centered on the impact point is displayed in the following figures. What is more, the range of legend values for the contour plot is set as 0.949–0.95 without interpolation of the damage variable, so the elements in red are considered to be completely failed. Last but not least, in our work, the interlaminar failure area size is employed to quantitatively evaluate the impact resistance of automotive coatings.

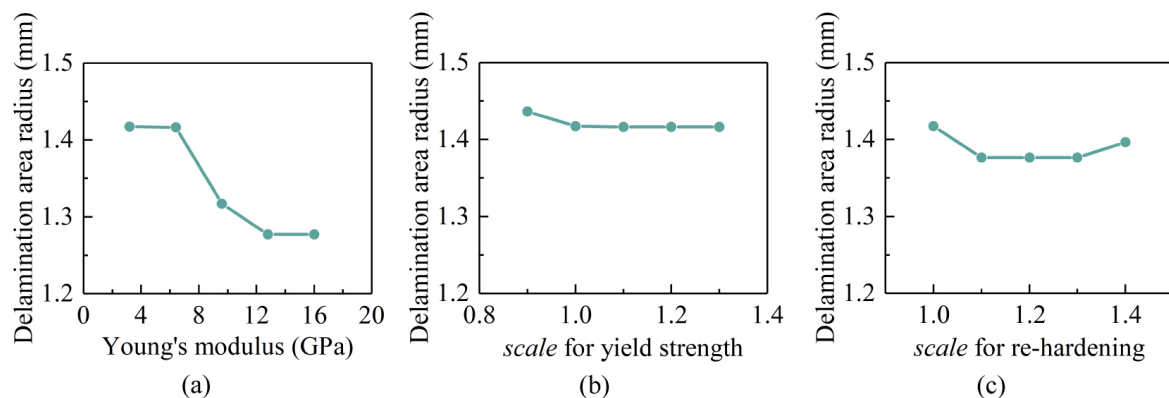### 4.1. The Effect of Young's Modulus

The polymer-ply failure patterns of automotive coatings with different Young's moduli of primer are exhibited in Figure 16. It should be mentioned that the damage degree of the clearcoat is tightly related to the outflow of the coating material. As can be seen, a higher Young's modulus means a stiffer primer, which limits the outflow of the coating material. Consequently, the damage degree of the clearcoat decreases with the increase of this parameter. In addition, a stiffer primer is less prone to plastic deformation; hence, the ductile damage of the primer is inhibited. Meanwhile, since the basecoat and electrocoat have failed, the undamaged primer needs to bear higher radial stresses induced by the coating buckling so that circumferential cracks occur in the primer.
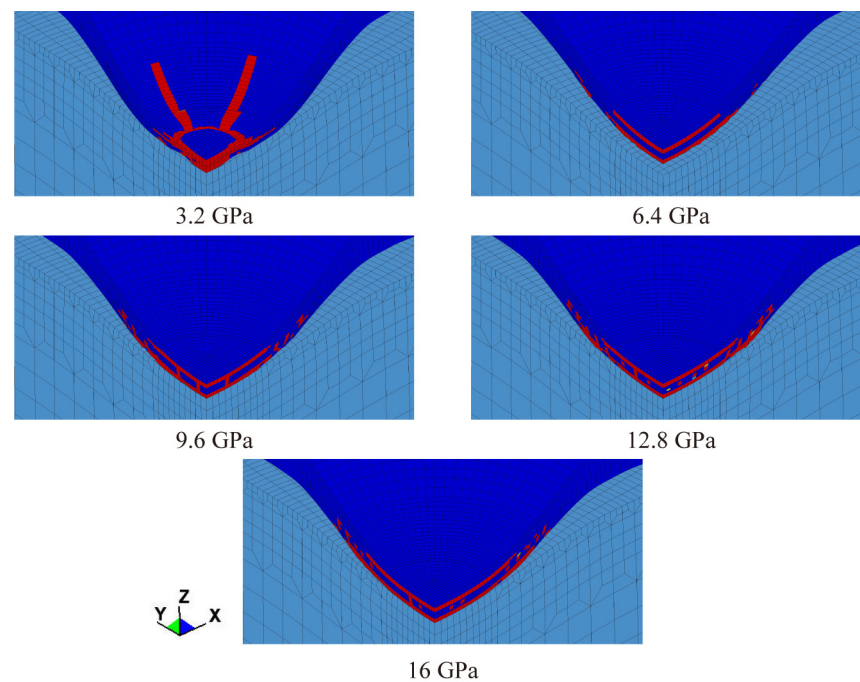
**Figure 16.** Final failure patterns of automotive coatings with different Young's moduli of primer.

The dependence of interlaminar failure on Young's modulus of the primer is presented in Figure 17a. As is shown, increasing Young's modulus of the primer results in a growth of the overall stiffness of the coating; hence, the degree of coating buckling is reduced, which leads to a decrease in the delamination area. However, when the modulus is large enough, this effect becomes weaker.

Figure 17. Dependence of the delamination area size on primer mechanical properties. (**a**) Young's modulus, (**b**) yield strength, and (**c**) re-hardening modulus.

4.2. The Effect of Yield Behavior

In this sub-subsection, we studied the effect of the yield behavior of the primer on the impact resistance of automotive coatings, focusing on the yield strength and re-hardening modulus. Considering that a piecewise-linear-plastic model is employed to characterize the mechanical behavior of the coating in our work, manipulation of $\sigma_{y,s} - \varepsilon_p$ data of the primer listed in Table 4 is needed. With reference to the method of Zou [36], the third value of $\sigma_{y,s}$ is considered as the yield strength, which is scaled by a parameter *scale*, and linear interpolation is performed to obtain the modified one of the second yield stress data. Except for these two values, the others are kept constant. As for the modification of the re-hardening modulus of the primer, the sixth value of $\sigma_{y,s}$ is scaled by the parameter *scale*, and the other data remain unchanged. The modified curves are plotted in Figure 18.

(a) Modification of yield strength (b) Modification of re-hardeniong modulus
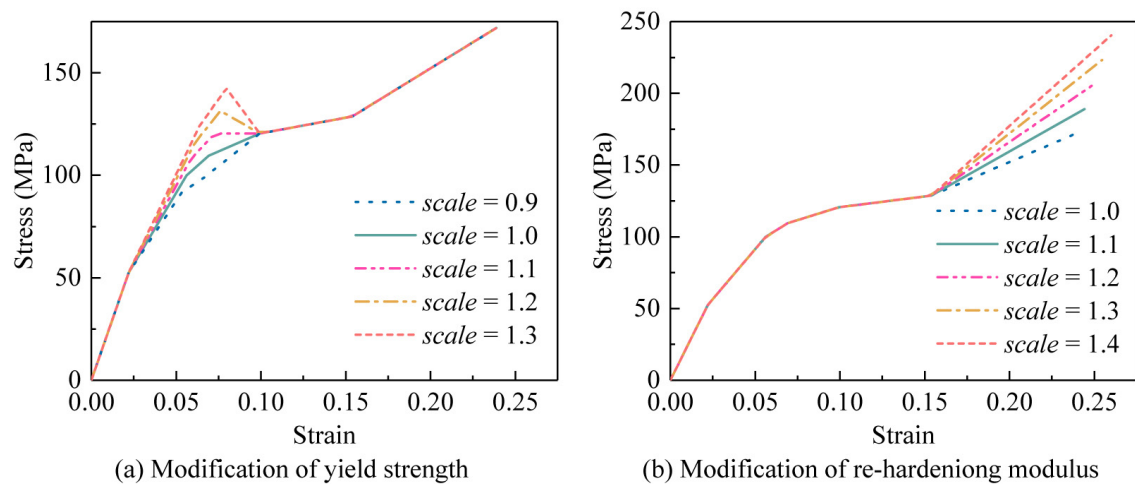
Figure 18. Stress–strain curve of primer at 5 s^{-1}. (**a**) Modification of yield strength. *scale* is the ratio of modified yield strength to its initial value. (**b**) Modification of re-hardening modulus. *scale* is the scale factor of the 6th value of yield stress in Table 4.

Figure 19 plots the polymer-ply damage patterns of automotive coatings with different yield strengths of the primer. As shown in the figure, the polymer-ply damage patterns with different yield strengths are largely similar. The dependence of interlaminar failure on the yield strength of the primer is shown in Figure 17b. If the result of *scale* = 1.0 is taken as the reference value, the maximum relative bias in the interlaminar failure area radius is only 1.36%. In other words, the yield strength of the primer has a minor influence on the impact response of automotive coatings. The analysis shows that when a particle impacts the coating at a high speed, the resulting von Mises effective stresses on the primer are far higher than its yield strength. Therefore, increasing the yield strength has little effect on the response of the primer under particle extrusion and makes little difference to the damage degree of coating.

scale = 0.9   scale = 1.0

scale = 1.1   scale = 1.2

scale = 1.3
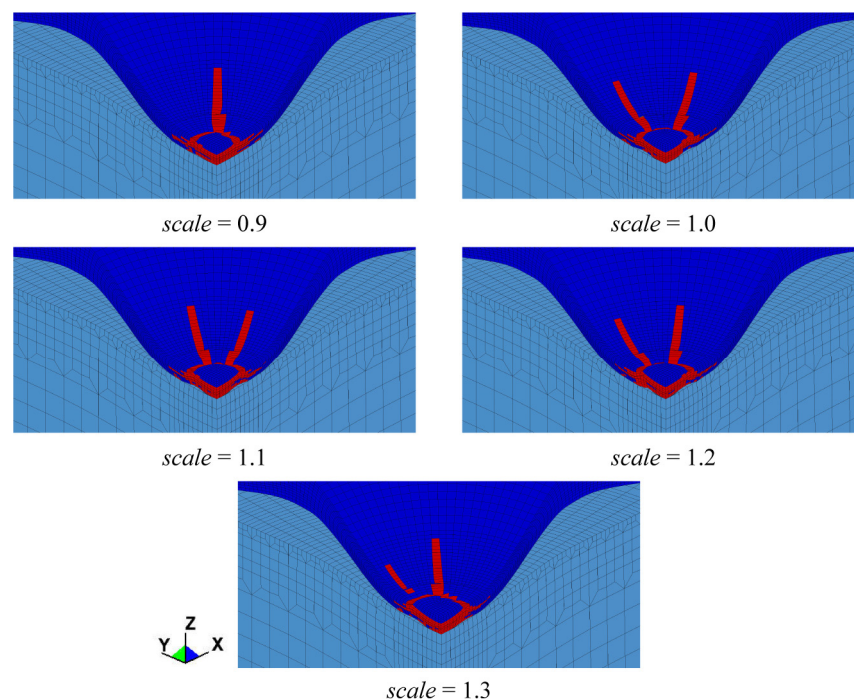
Figure 19. Final failure patterns of automotive coatings with different yield strengths of primer.

Failure patterns of the coating systems with different re-hardening moduli are illustrated in Figure 20. It is noted that damage of the primer is sensitive to the re-hardening modulus, and a slight increase in the re-hardening modulus will result in no damage to the primer. This is attributed to the fact that a larger re-hardening modulus corresponds to a stiffer curve in the re-hardening phase of the primer; hence, the ductile failure of the primer is inhibited. At the same time, the outflow of coating material is limited due to the undamaged primer, so the damage degree of clearcoat is alleviated.

scale = 1.0   *scale* = 1.1

scale = 1.2   *scale* = 1.3

scale = 1.4
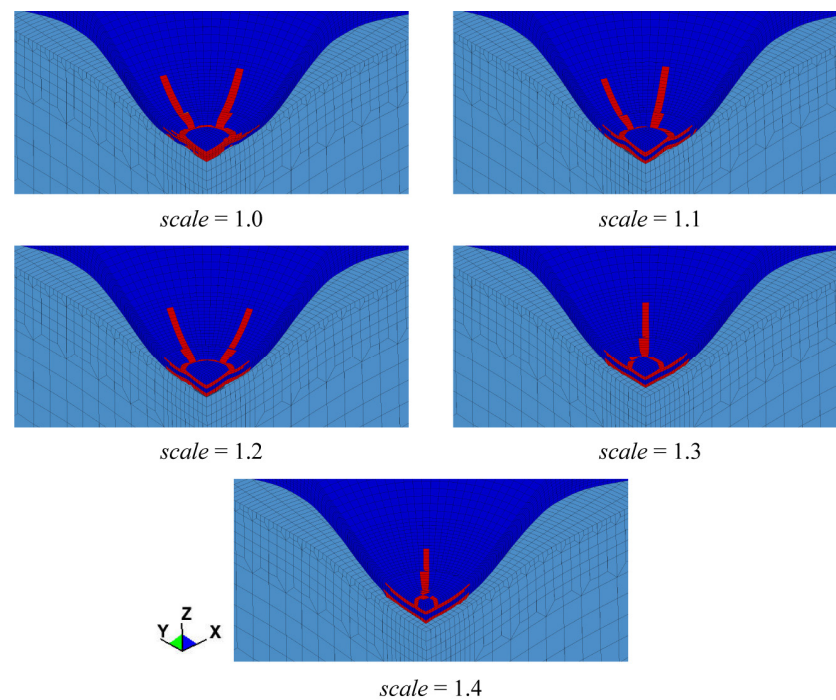
Figure 20. Final failure patterns of automotive coatings with different re-hardening moduli of primer.

The influence of the re-hardening modulus on the delamination area is given in Figure 17c. As analyzed above, a slight increase of the re-hardening modulus will result in no damage to the primer, and then the outward flow of the coating material is restricted and the coating buckling degree decreases. Therefore, when the *scale* = 1.1, a reduction in delamination area size is observed. After that, the further growth of this parameter cannot change the damage state of the primer, so the interlaminar failure degree keeps constant. In other words, when the re-hardening modulus reaches a certain value, the effect of further increasing this parameter on the impact failure of automotive coatings is negligible.

5. Conclusions

In this paper, a finite element model is developed for the single-impact failure of automotive coatings. In this model, both polymer-ply and interlaminar failures of the coating are considered, and the results show that with appropriate parameters, the simulation can reproduce the impact failure patterns of the automotive coating well, which can potentially support the development of higher-fidelity models. In addition, the proposed model can qualitatively capture the effect of impact velocity.

The impact failure mechanisms of coating are numerically revealed. Results show that both brittle and ductile failure can be found in the coating. In addition, there are three stages for the propagation of the delamination crack. Firstly, during the particle pressing process, the shear stress dominates the initiation of damage. Secondly, when the particle moves backward, the radial compressive stress motivates the coating material to flow outward, which makes the delamination crack propagate outward in a mixed mode. Finally, after the particle disengages from the coating, the out-of-sync vibrations between the coating and the substrate aggravate the interlaminar failure.

The effects of primer mechanical properties on the impact resistance of automotive coatings are studied. The main numerical findings are summarized as follows:

1. The increase of Young's modulus can significantly improve the impact resistance of automotive coatings, which is manifested as the negative correlation between the interlaminar failure area and Young's modulus.

2. Since the resulting von Mises effective stresses on the primer are far higher than its yield strength during the single-impact process, changing the yield strength does not affect the impact resistance of automotive coatings.

3. Damage of the primer is sensitive to the re-hardening modulus, and a slight increase in the re-hardening modulus will result in no damage to the primer. However, when the re-hardening modulus reaches a certain value, the effect of further increasing the re-hardening modulus on the impact failure of automotive coatings is negligible.

There are still several points that need to be addressed in the current study. The first is the problem of parameter identification and developing a reliable parameter identification method is an essential step to make it a model of higher fidelity. Secondly, the parametric results show that Young's modulus of the primer has a great influence on the impact response of the automotive coating, which indicates that we should consider the viscoelastic properties of the polymer in subsequent studies. Lastly, to achieve quantitative prediction of the influence of impact velocity, some improvements of this model are needed. All of the above will be our key research directions in the future.

References

1. *DIN 55996-1*; Paints and Varnishes—Stone Chip Resistance Test for Coatings—Part 1: Multi Impact Test. Deutsches Institut fur Normung e.V: Berlin, Germany, 2001.

2. *SAE J400*; Test for Chip Resistance of Surface Coatings. Society of Automotive Engineers: New York, NY, USA, 2002.

3. Zhaoyong, H. Experimental Study on Mechanical Properties of Automotive Body Coatings. Postgraduate's Thesis, South China University of Technology, Guangzhou, China, 2020.

4. Trezona, R.I.; Hutchings, I.M. Resistance of paint coatings to multiple solid particle impact: Effect of coating thickness and substrate material. *Prog. Org. Coat.* **2001**, *41*, 85–92. [CrossRef]

5. Maozhong, Y.; Baiyun, H.; Jiawen, H. Erosion wear behaviour and model of abradable seal coating. *Wear* **2002**, *252*, 9–15. [CrossRef]

6. Wood, R.J.K. The sand erosion performance of coatings. *Mater. Des.* **1999**, *20*, 179–191. [CrossRef]

7. Razin, A.A.; Ramezanzadeh, B.; Yari, H. Detecting and estimating the extent of automotive coating delamination and damage indexes after stone chipping using electrochemical impedance spectroscopy. *Prog. Org. Coat.* **2016**, *92*, 95–109. [CrossRef]

8. Nichols, M.E.; Misovski, T. 3—Instrumented stone chipping of automotive paint systems. In *Service Life Prediction of Polymers and Coatings*; White, C.C., Nichols, M.E., Pickett, J.E., Eds.; William Andrew Publishing: New York, NY, USA, 2020; ISBN 978-0-12-818367-0.

9. Liu, Y.; Zou, C.; Zang, M.; Chen, S. Experimental study on mechanical property and stone-chip resistance of automotive coatings. *Mater. Res. Express* **2022**, *9*, 16402. [CrossRef]

10. Zehnder, A.T.; Ramamurthy, A.C.; Bless, S.J.; Brar, N.S. Stone impact damage to automotive paint finishes: Measurement of temperature rise due to impact. *Int. J. Impact Eng.* **1993**, *13*, 133–143. [CrossRef]

11. Ramamurthy, A.C.; Lorenzen, W.I.; Bless, S.J. Stone impact damage to automotive paint finishes: An introduction to impact physics and impact induced corrosion. *Prog. Org. Coat.* **1994**, *25*, 43–71. [CrossRef]

12. Eraky, M.T.; Elmelegy, T.; Shazly, M.; Eltayeb, N.S.M. A combined CFD-SOLID finite element model to study the mechanics of sand erosion damage in coated glass fiber reinforced polymer. In Proceedings of the International Mechanical Engineering Congress and Exposition, Pittsburgh, PA, USA, 9–15 November 2018.

13. Xiong, S.; Chen, S.; Zang, M.; Makoto, T. Development of an Unresolved CFD-DEM Method for Interaction Simulations Between Large Particles and Fluids. *Int. J. Comput. Methods* **2021**, *18*, 2150047. [CrossRef]

14. Qian, J.; Zou, C.; Zang, M.; Chen, S.; Tsubokura, M. A CFD-DEM-Wear Coupling Method for Stone Chip Resistance of Automotive Coatings with a Rigid Connection Particle Method for Non-Spherical Particles. *Comput. Model. Eng. Sci.* **2022**, *133*, 251–280. [CrossRef]

15. Xiao, G. Research on the Mechanism of Anti-Stone-Damage Automotive Coating Based on Computational Fluid Dynamics Method. *Coatings* **2022**, *12*, 295. [CrossRef]

16. Toi, Y.; Park, J.; Nakai, N.; Hara, Y. Identification of Dynamic Damage Mechanics Models and Tensile Fracture Analysis for Multi-Layer Coatings. *Trans. Jpn. Soc. Mech. Eng. Ser. A* **2005**, *71*, 1626–1631. [CrossRef]

17. Xian, Y.; Toi, Y. Damage Mechanics Simulation of Dynamic Fracture Behaviors of Multi-Layer Coatings by Uncoupled Analysis. *Trans. Jpn. Soc. Simul. Technol.* **2016**, *8*, 119–127.

18. Grujicic, M.; Pandurangan, B.; He, T.; Cheeseman, B.A.; Yen, C.F.; Randow, C.L. Computational investigation of impact energy absorption capability of polyurea coatings via deformation-induced glass transition. *Mater. Sci. Eng. A* **2010**, *527*, 7741–7751. [CrossRef]

19. Zhang, J.; Wang, C.Q.; Kan, Q.H. Finite element analysis for impact debonding mechanisms of polymer coating. *Sichuan Daxue Xuebao (Gongcheng Kexue Ban)/J. Sichuan Univ. (Eng. Sci. Ed.)* **2012**, *44*, 122–125.

20. Xu, X.; Zou, C.; Zang, M.; Chen, S. Development of a GPU parallel computational framework for impact debonding of coating-substrate interfaces. *Thin-Walled Struct.* **2022**, *175*, 109270. [CrossRef]

21. Zhang, N.; Yang, F.; Li, L.; Shen, C.; Castro, J.; Lee, L.J. Thickness effect on particle erosion resistance of thermoplastic polyurethane coating on steel substrate. *Wear* **2013**, *303*, 49–55. [CrossRef]

22. Gong, Y.; Yang, Z.; Wang, Y. Impact Simulation on Ductile Metal Pipe with Polymer Coating by a Coupled Finite Element and Meshfree Method. *J. Fail. Anal. Prev.* **2012**, *12*, 267–272. [CrossRef]

23. Zhang, H.; Li, Z.; He, W.; Liao, B.; He, G.; Cao, X.; Li, Y. Damage evolution and mechanism of TiN/Ti multilayer coatings in sand erosion condition. *Surf. Coat. Technol.* **2018**, *353*, 210–220. [CrossRef]

24. Fallon, C.; Mcshane, G.J. Design of elastomer coatings for concrete impact damage mitigation. *Int. J. Impact Eng.* **2020**, *146*, 103700. [CrossRef]

25. Liu, Y.; Liaw, B. Drop-weight impact tests and finite element modeling of cast acrylic/aluminum plates. *Polym. Test* **2009**, *28*, 808–823. [CrossRef]

26. Zouari, B.; Touratier, M. Identification of an elasto-viscoplastic flow stress in large strains and large strain rates of a paint film from impacts. *Int. J. Form. Process.* **2005**, *2–3*, 227–249. [CrossRef]

27. Cen, H.; Tian, W.; Li, P.; Wei, R. Simulation Analysis on Polyurethane Coating of Wind Blade. *J. Shanghai Jiaotong Univ. (Sci.)* **2019**, *24*, 496–499. [CrossRef]

28. Zouari, B.; Touratier, M. Simulation of organic coating removal by particle impact. *Wear* **2002**, *253*, 488–497. [CrossRef]

29. Zou, C.; Yang, H.; Xu, X.; Zang, M.; Chen, S. Computational modeling of impact failure of polymer coatings. *Compos. Struct.* **2022**, *291*, 115576. [CrossRef]

30. Chen, D.; Sarumi, M.; Al-Hassani, S.T.S.; Gan, S.; Yin, Z. A model for erosion at normal impact. *Wear* **1997**, *205*, 32–39. [CrossRef]

31. Aquaro, D.; Fontani, E. Erosion of ductile and brittle materials. *Meccanica* **2001**, *36*, 651–661. [CrossRef]

32. Finnie, I. Some observations on the erosion of ductile metals. *Wear* **1972**, *19*, 81–90. [CrossRef]

33. Papini, M.; Spelt, J.K. The plowing erosion of organic coatings by spherical particles. *Wear* **1998**, *222*, 38–48. [CrossRef]

34. Ramamurthy, A.C.; Buresh, G.A.; Nagy, M.; Howell, M. Novel instrumentation for evaluating stone impact wear of automotive paint systems. *Wear* **1999**, *225–229*, 936–948. [CrossRef]

35. Papini, M.; Spelt, J.K. Organic coating removal by particle impact. *Wear* **1997**, *213*, 185–199. [CrossRef]

36. Zou, C.; Guo, X.; Xu, X.; Zang, M.; Chen, S. Large deformation delamination in polymer coatings: Discontinuous Galerkin/cohesive zone modeling. *Int. J. Mech. Sci.* **2022**, *232*, 107635. [CrossRef]

37. Wonnemann, H. *Primer Surfacer*; John Wiley & Sons, Ltd.: New York, NY, USA, 2008; pp. 129–174.

38. Zhengyi, L. Testing and Analysis of Mechanical Properties for Automotive Coatings. Postgraduate's Thesis, Southwest Jiaotong University, Chengdu, China, 2009.

39. Lonyuk, M.; Bosma, M.; Vijverberg, C.A.M.; Bakker, A.; Janssen, M. Relation between chip resistance and mechanical properties of automotive coatings. *Prog. Org. Coat.* **2008**, *61*, 308–315. [CrossRef]

40. Lonyuk, M.; Bosma, M.; Riemslag, A.C.; Zuidema, J.; Bakker, A.; Janssen, M. Stone-impact damage of automotive coatings: A laboratory single-impact tester. *Prog. Org. Coat.* **2007**, *58*, 241–247. [CrossRef]

41. Li, C.; Chenqi, Z.; Mengyan, Z. Simulation Analysis of Impact Damage of Automotive Coatings. In Proceedings of the China SAE Congress and Exhibition (SAECCE), Shanghai, China, 22–24 November 2022.

42. Nguyen, V.D.; Lani, F.; Pardoen, T.; Morelle, X.P.; Noels, L. A large strain hyperelastic viscoelastic-viscoplastic-damage constitutive model based on a multi-mechanism non-local damage continuum for amorphous glassy polymers. *Int. J. Solids Struct.* **2016**, *96*, 192–216. [CrossRef]

43. Jirásek, M.; Bauer, M. Numerical aspects of the crack band approach. *Comput. Struct.* **2012**, *110–111*, 60–78. [CrossRef]

44. Skamniotis, C.G.; Elliott, M.; Charalambides, M.N. On modelling the constitutive and damage behaviour of highly non-linear bio-composites—Mesh sensitivity of the viscoplastic-damage law computations. *Int. J. Plast.* **2019**, *114*, 40–62. [CrossRef]

45. Lemaitre, J.; Desmorat, R. *Engineering Damage Mechanics: Ductile, Creep, Fatigue and Brittle Failures*; Springer Science & Business Media: New York, NY, USA, 2006; ISBN 3540272933.

46. Fleck, N.A.; Stronge, W.J.; Liu, J.H. High strain-rate shear response of polycarbonate and polymethyl methacrylate. *Proc. R. Soc. Lond. A Math. Phys. Sci.* **1990**, *429*, 459–479.

47. Gerlach, R.; Siviour, C.R.; Petrinic, N.; Wiegand, J. Experimental characterisation and constitutive modelling of RTM-6 resin under impact loading. *Polymer* **2008**, *49*, 2728–2737. [CrossRef]

48. Mirghaderi, H.; Rahbar Ranji, A.; Fadavie, M. The effect of epoxy coating on the fatigue strength of grade-A mild steel. *J. Adhes. Sci. Technol.* **2021**, *36*, 1847–1857. [CrossRef]

49. Islam, M.S.; Tong, L. Effects of initial blister radius and shaft diameter on energy release rate of metal-polymer composite coating. *Int. J. Adhes. Adhes.* **2015**, *62*, 107–123. [CrossRef]

50. Zou, Z.; Lee, H. A cohesive zone model taking account of the effect of through-thickness compression. *Compos. Part A Appl. Sci. Manuf.* **2017**, *98*, 90–98. [CrossRef]

51. Fischer, K.A.; Wriggers, P. Frictionless 2D Contact formulations for finite deformations based on the mortar method. *Comput. Mech.* **2005**, *36*, 226–244. [CrossRef]

52. Farah, P.; Popp, A.; Wall, W.A. Segment-based vs. element-based integration for mortar methods in computational contact mechanics. *Comput. Mech.* **2015**, *55*, 209–228. [CrossRef]

53. Ryntz, R.A.; Everson, M. Friction induced paint damage as affected by clearcoat chemistry. *Prog. Org. Coat.* **1997**, *31*, 281–288. [CrossRef]

54. Ledbetter, H.M.; Weston, W.F.; Naimon, E.R. Low-temperature elastic properties of four austenitic stainless steels. *J. Appl. Phys.* **1975**, *46*, 3855–3860. [CrossRef]

55. Ledbetter, H.M.; Frederick, N.V.; Austin, M.W. Elastic-constant variability in stainless-steel 304. *J. Appl. Phys.* **1980**, *51*, 305–309. [CrossRef]

56. Xingxing, W.; Jianhu, L.; Lunping, Z.; Liping, M.; Jun, W. Numerical simulation analysis of petaling formation process of plate penetrated by sharp-nosed missile. *Chin. J. Ship Res.* **2018**, *3*, 110–117.

57. Rumzan, I.; Williams, J.G. Compressive stress-strain properties of automotive paints over a range of strain rates and temperatures. *Polymer* **2000**, *41*, 4291–4307. [CrossRef]

58. Jordan, J.L.; Foley, J.R.; Siviour, C.R. Mechanical properties of Epon 826/DEA epoxy. *Mech. Time-Depend. Mater.* **2008**, *12*, 249–272. [CrossRef]